

PAPER

Self-sensing electromagnetic shunt damper for adaptive vibration control

To cite this article: Qiheng Xu et al 2025 Smart Mater. Struct. 34 105021

View the article online for updates and enhancements.

You may also like

Bastos et al.

- Photonic-digital hybrid artificial intelligence hardware architectures: at the interface of the real and virtual worlds
 Lília M S Dias, Dinis O Abranches, Ana R
- ICRH modelling of DTT in full power and reduced-field plasma scenarios using full wave codes
- A Cardinali, C Castaldo, F Napoli et al.
- Low-noise anisotropic magnetoresistance sensing at human body temperature: unveiling the optimal doping in La_Sr_MnO_films
 Raul Solis Leon, Ines Garcia Manuz,
 Sandeep Kumar Chaluvadi et al.



Smart Mater. Struct. 34 (2025) 105021 (15pp)

https://doi.org/10.1088/1361-665X/ae0d1b

Self-sensing electromagnetic shunt damper for adaptive vibration control

Qiheng Xu¹, Ruqi Sun^{2,*}, Yongjia Liu², Qian Li³ and Li Cheng⁴

E-mail: sunruqi@chd.edu.cn

Received 14 August 2025, revised 14 September 2025 Accepted for publication 28 September 2025 Published 16 October 2025



Abstract

The self-sensing damper is an effective vibration suppression actuator, particularly in scenarios where installing additional sensors is prohibited. This study proposes a self-sensing electromagnetic shunt damper to improve the linear model-based velocity prediction accuracy and extricate the heavy dependence on external sensors. By introducing a gradient boosting regression (GBR) model with feature-engineered voltage signals, lagged derivatives, and polarity information for data-driven velocity inference, the prediction error is reduced by 14% versus the traditional GBR model. The model is optimized and pruned via cross-validated grid search to fit 32 KB microcontroller flash memory, enabling real-time computation. An integrated balance logic algorithm is then adopted for energy-efficient adaptive control with the adjusted load resistance based on the predicted velocity. Moreover, the experimental results with swept sinusoidal excitation confirm the high-precision velocity prediction accuracy and effective vibration suppression performance. This sensor-free and low-cost solution simplifies system architecture, reduces installation complexity, thereby holding great promise for broad applications in civil engineering, automotive engineering, and precision machinery.

Keywords: self-sensing actuator, electromagnetic shunt damper, velocity prediction, adaptive vibration control

Nomenclature

EMF Electromotive force
EMSD Electromagnetic shunt damper
GBR Gradient boosting regression
MCU Microcontroller unit
MI Mutual information
RFE Recursive feature elimination

RMS Root mean Square
RMSE Root mean square error
SDOF Single-degree-of-freedom
SHAP Shapley additive explanations

SS-EMSD Self-sensing electromagnetic shunt damper

1. Introduction

Ranging from precision instrumentation and seismic mitigation to mechanical system design, vibration suppression remains a critical determinant of performance, reliability, and service life across applications. Conventional passive strategies, while structurally simple and inherently stable, often struggle to reconcile efficiency with adaptability under complex and variable dynamics. This has shifted attention to semi-active control with tunable damping-particularly the EMSD, which employs adjustable resistor networks to modulate damping on demand and offers prospects for self-powered operation.

Over recent years, EMSD development has followed two prominent trends: bidirectional energy-damping flow and

¹ School of Mechanical and Automotive Engineering, South China University of Technology, Guangzhou 510641, People's Republic of China

² School of Automobile, Chang'an University, Xi'an 710018, People's Republic of China

³ Yi-Tong UAV System Co., Ltd, Yantai 264000, People's Republic of China

⁴ Department of Mechanical Engineering, The Hong Kong Polytechnic University, Hong Kong Special Administrative Region of China 990777, People's Republic of China

^{*} Author to whom any correspondence should be addressed.

tunable electromechanical coupling. Li and Zhu [1] proposed a hybrid bidirectional energy-regenerative electromagnetic damper with synthetic impedance that emulates multiple conventional devices while harvesting energy. Shen et al [2] integrated inerters into a tuned electromagnetic damper to enhance tunability and generate electrical energy on a full-scale cable test. For structural and base isolation, Li et al [3] coupled eddycurrent damping with inertial effects in tuned mass damperinerter systems, Sun et al [4, 5] developed quasi-zero-stiffness Gough-Stewart isolation platforms with active control. In automotive engineering, Tan et al [6] realized semi-active suspensions capable of simultaneously modulating damping and inertial forces, showing superior multi-band performance over hydraulic counterparts. Moreover, self-sensing windings have been embedded into electromagnetic shunt dampers to unify damping and velocity measurement [7], and Zaccardo and Buckner [8] addressed position-estimation errors from magnetic saturation and duty-cycle variation in active magnetic dampers. With interdisciplinary mechanisms such as triboelectric energy harvesting and artificial intelligence, Cui et al [9] developed adaptive vibration suppression-energy harvesting systems, while Tang et al [10] integrated AI-driven magnetic-friction hybrid generators with structural-state identification for train vibration monitoring. These efforts lay a foundation for multifunctional, multiphysics-coupled EMSD technologies, yet they also expose a continuing reliance on internal state awareness-motivating the following discussion on self-sensing techniques.

For self-sensing capacity, the goal is to acquire structural state and actuation signals without external sensors. Shen et al [11] used piezoelectric elements to harvest energy while detecting optimal switching instants, overcoming timing delays inherent in synchronized switching damping on inductor systems. Qin et al [12] transplanted a permanentmagnet synchronous motor model into a semi-active EMSD to estimate displacement and velocity online. Earlier, Hong and Pang reduced modal amplitudes by 50%-75% in dual-stage hard-disk suspensions using indirect drive-based approaches [13], and Freyer et al [14] validated around 10 dB attenuation at a tool's primary mode via hardware-in-the-loop selfsensing control. Since then, applications have expanded rapidly: Li et al [15] developed an ultrasonic elliptical-vibration cutting system with real-time tool-path estimation; Mao and Dankowicz [16] exploited amplitude ratios of coupled oscillators for nanoscale mass detection; Li et al [17] combined digital-twin modeling with SVM-based self-sensing slidingmode control to suppress chatter in high-dynamic machining. With actuator functionality, Chang et al [18] introduced an impedance-current estimation method, and Hu et al [19] proposed a two-dimensional compensation strategy advancing piezoelectric actuators toward fully closed-loop, selfsensing active control. Collectively, these studies show that self-sensing can deliver sufficiently accurate state information to underpin real-time adaptive control.

For semi-active strategies, researchers have combined self-sensing with intelligent algorithms and reconfigurable

structural units to approach a low-power, high-performance paradigm. Piezoelectric circuit systems, such as synchronized switch damping on voltage sources [20] and on negative capacitance [21], achieve significant damping with milliwattlevel power via synchronized switching. Jiang et al [22] utilized data-driven model identification for low-frequency vibration control. In industrial robotics, Neubauer et al [23] applied an H_{∞} co-design strategy to reduce trajectorytracking errors by 42.7%, while Zhang et al [24] used an LSTM prediction-fuzzy control framework to coordinate seismic mitigation of adjacent tall buildings. To accommodate long-span or complex structures, co-evolving devices and algorithms have been explored, including cross-floor cablebased displacement amplification [25], the unconditionally stable SSE- α integration scheme [26], bio-inspired structures [27], and high-utilization displacement amplification devices [28]. Meanwhile, high-damping cables [29], nonlinear tool-damper coupling [30], and centrifugal pendulummixed mechanisms [31] broaden operating bandwidths and load ranges. Cross-domain integration with energy harvesting is also accelerating: bio-inspired structures [32], monostable harvesters [33], bistable harvesters [34], tristable harvesters [35], hybrid train-based energy collection systems [36], and magnetorheological elastomer-based absorbers [37] all validate the feasibility of closed-loop systems that couple selfsensing, energy supply, and damping tuning. Beyond classical platforms, Tian et al [38] applied self-parametric optimization to quantum sensing for low-frequency active vibration isolation.

Despite these advances, the deployment of EMSD in advanced applications still faces two principal challenges. First, traditional linear models are inadequate to capture the strongly nonlinear coupling between induced coil voltage and relative velocity, leading to prediction errors. Second, dependence on external displacement or acceleration sensors inflates hardware cost, system complexity, power consumption, and installation difficulty in space-constrained settings. To address these issues, this study proposes a SS-EMSD framework that integrates data-driven modeling with embedded real-time control, aiming to improve vibration suppression while simplifying system architecture. The key innovations of this work are threefold:

- (1) Nonlinear mapping via GBR: the GBR algorithm is applied in the proposed SS-EMSD, employing feature engineering and lagged-term combinations to accurately characterize the complex voltage-velocity relationship. This method reduces the prediction error by 14% compared with the traditional GBR method.
- (2) Prediction optimization through hyperparameter tuning and model pruning: a system optimization approach that includes cross-validated hyperparameter search and lightweight model pruning is implemented, thereby striking a balance between the predictive performance and the resource requirement. This ensures the GBR

model achieves minimal error while meeting the stringent memory and computation constraints of embedded platforms.

(3) Embedded adaptive damping control logic: by compressing and porting the optimized GBR model into resource-constrained microcontrollers (e.g. Arduino), millisecond-scale velocity prediction and online damping-force adjustment are realized. This self-sensing scheme eliminates dependency on external sensors, simplifies the control architecture, and reduces energy consumption.

This paper provides the theoretical analysis of the selfsensing real-time control for EMSDs and the experimental verification of the semi-active vibration control performance with the proposed SS-EMSD, thereby offering new directions for future developments in precision vibration mitigation. This paper provides the theoretical foundation and experimental validation of a self-sensing real-time control framework for EMSDs, aiming to enable sensor-free, adaptive vibration mitigation. The rest of the paper is organized as follows. Section 2 introduces the self-sensing mechanism and the associated damping control logic. Section 3 presents the experimental setup and system identification procedure. Section 4 discusses the test results under various operating conditions to evaluate both sensing accuracy and vibration suppression performance. Section 5 concludes the paper with a summary of findings and future perspectives.

2. Design and modeling

This section elaborates on the working principle and modeling method of the proposed SS-EMSD. Firstly, the mechanism and theoretical basis of electromagnetic damping and force tracking control are introduced. Then, the GBR procedure is derived in detail to predict the relative velocity accurately. Moreover, the real-time damping control algorithm of the system is also interpreted.

2.1. Tunable EMSD

For EMSDs, Faraday's law of induction underpins the energy conversion from mechanical motion into electrical power. When a conductor with the effective length l moves at the velocity of v through the magnetic flux density \mathcal{B} , the resulting EMF is

$$\varepsilon = Blv.$$
 (1)

In principle, if the conductor moves in a spatially varying magnetic field $\mathcal{B}_r(x,r)$ at velocity \dot{x} , the induced EMF is given by

$$\varepsilon = -\oint \mathcal{B}_r(x, r) \, \mathrm{d}l\dot{x},\tag{2}$$

which highlights the two influence factors of the EMF: the magnetic flux density and the relative velocity.

The transduction factor K_t is a key parameter describing how the mechanical energy is converted into electrical energy. For a single loop, it can be written as

$$K_{t} = -\oint \mathcal{B}_{r}(x, r) \, \mathrm{d}l. \tag{3}$$

For the entire coil (with length l_{wire} and cross-sectional area A_{cross}), it often involves the integration of the magnetic flux density over the coil region:

$$K_{\rm t} = -\frac{l_{\rm wire}}{A_{\rm cross}} \int_{r_1}^{r_2} \int_{x_1}^{x_2} \mathcal{B}_r(x, r) \, \mathrm{d}x \, \mathrm{d}r.$$
 (4)

When the coil is connected to an external resistor R_{load} , the combination of coil resistance R_{in} and R_{load} yields the circuit impedance Z. The EMSD then exerts an equivalent damping force on the vibrating structure:

$$F_{\rm e} = \frac{K_{\rm t}^2}{Z} \dot{z},\tag{5}$$

where \dot{z} is the relative velocity between the coil and the magnetic column. For a purely resistive circuit with total resistance $R_{\rm in}$ and $R_{\rm load}$, the damping coefficient $c_{\rm e}$ becomes

$$c_{\rm e} = \frac{K_{\rm t}^2}{R_{\rm in} + R_{\rm load}}.\tag{6}$$

As shown in figure 1(a), several N32 NdFeB ring-shaped permanent magnets are utilized to build the opposing magnetic column in this study. The inner hole diameter of the magnet is 5 mm, the outer diameter is 35 mm, and the thickness is 6 mm. Two magnets are arranged in opposite polarities with screwnuts so that the two S magnetic poles are physically connected in figure 1. The magnetic flux density with the arranged magnet column is simulated using a magnetic analysis software for the transduction factor K_t calculation. Moreover, the induction coil is fabricated from high-purity enameled copper wire with a diameter of 1.2 mm and an overall wound length of 120 mm, ensuring a low-resistance path and high sensitivity to motion-induced EMF in the core region.

2.2. Self-sensing with GBR model

Since the EMF is related to the relative velocity, the EMSD velocity is possible to be obtained by the real-time measured voltage u of the external resistor R_{load} . The relationship between the relative velocity \dot{z} and the measured voltage u can be expressed by

$$\dot{z} = \frac{u}{K_t \left(\frac{R_{\text{load}}}{R_{\text{in}} + R_{\text{load}}}\right)}.$$
 (7)

To obtain a more accurate measure of the SS-EMSD velocity, a data-driven model based on GBR in figure 2 is proposed for real-time prediction of relative velocity from the induced voltage. Suppose N discrete samples are collected, denoted $\{t_i, u_i, v_i\}_{i=1}^{N}$, where t_i is the time step, u_i is the coil voltage,

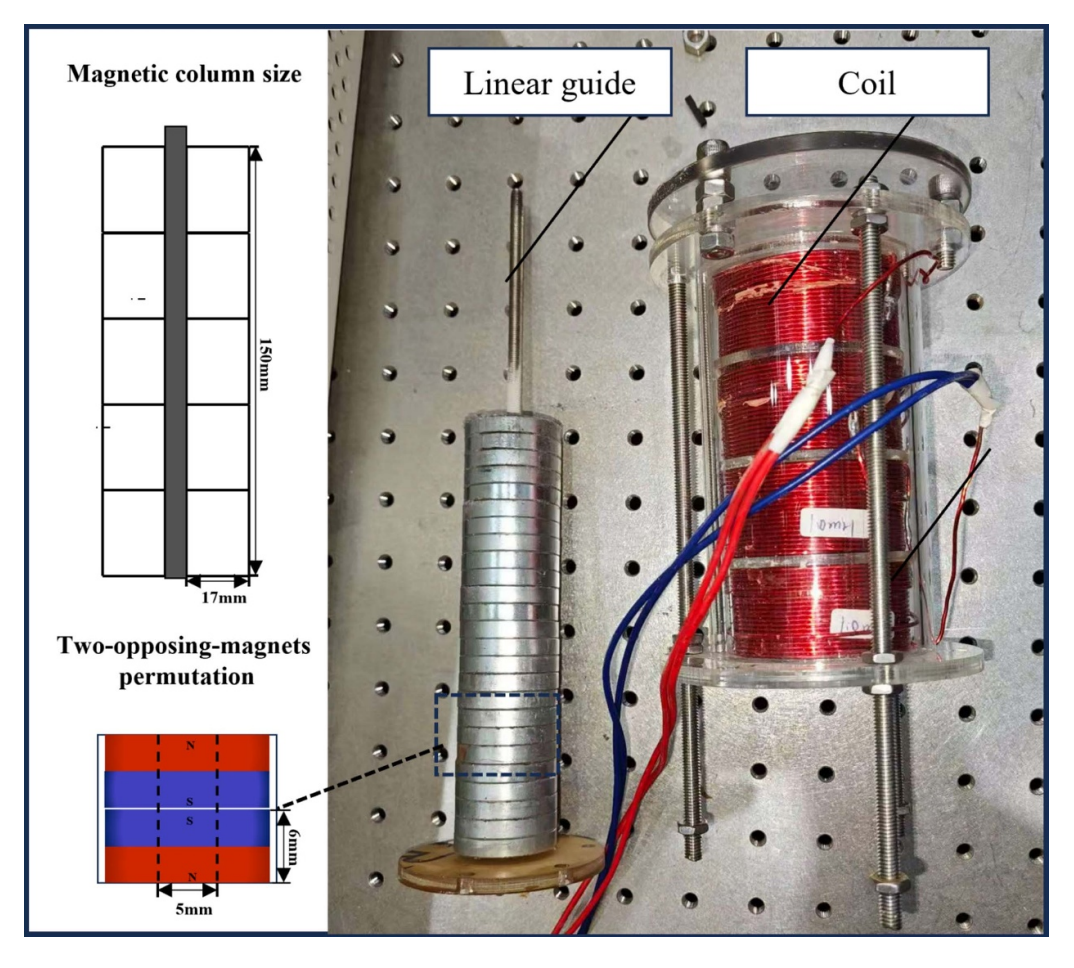


Figure 1. Detailed schematic diagram of the magnetic column structure of the electromagnetic damper prototype.

and v_i is the ground-truth relative velocity measured by a high-precision laser displacement sensor. Because the velocity changes only moderately within each interval $[t_{i-1}, t_i]$, the time derivative of the voltage is approximated by a backward difference

$$\dot{u}_i = \frac{u_i - u_{i-1}}{\Delta t_i}, \ \Delta t_i = t_i - t_{i-1}, i \ge 2, \ \dot{u}_1 = 0$$
 (8)

Because practical electromagnetic dampers exhibit memory and lag effects, the feature vector X_i is augmented with lagged terms up to order L = 4:

$$X_{i} = [u_{i}, \dot{u}_{i}, \operatorname{sgn}(\dot{u}_{i}), u_{i-1}, \dot{u}_{i-1}, \dots, u_{i-L}, \dot{u}_{i-L}]^{\top} \in \mathbb{R}^{3+2L}.$$
(9)

If $i \le L$, insufficient lags are padded with the initial voltage u_1 and $\dot{u}_1 = 0$, preventing boundary information loss. The sign function $\mathrm{sgn}\,(\dot{u}_i)$ is used to classify the instantaneous motion into rising, steady, or falling phases, thereby capturing the directional dependence inherent in electromagnetic hysteresis. This representation retains the instantaneous magnitude and slope of the voltage while encoding the non-stationary, path-dependent characteristics of the system simultaneously.

For regression, a gradient-boosted ensemble of regression trees with squared-error loss is adopted. For each training

sample set \mathcal{D}_{tr} the model output is

$$\hat{v}_i = \sum_{m=1}^{M} \eta h_m(\mathbf{X}_i; \alpha_m), \ 0 < \eta < 1,$$
 (10)

where h_m is a classification and regression tree of depth at most 3, M is the number of base learners, and η is the learning rate; and each tree is trained on a random subsample of size ratio S to mitigate overfitting. The parameter set $\theta = \{\alpha_m\}_{m=1}^M$ minimizes the empirical risk $\mathcal{L}(\theta)$:

$$L(\theta) = \frac{1}{|\mathcal{D}_{tr}|} \sum_{i \in \mathcal{D}_{tr}} (v_i - \hat{v}_i(\mathbf{X}_i; \theta))^2.$$
 (11)

The model performance on the independent test set \mathcal{D}_{te} is quantified by the RMS error

RMSE =
$$\sqrt{\frac{1}{|\mathcal{D}_{tE}|} \sum_{i \in \mathcal{D}_{te}} (v_i - \hat{v}_i)^2}$$
. (12)

To qualify the model predictions performance with the true values, the coefficient of determination R^2 can be defined as:

$$R^{2} = 1 - \frac{\sum_{i \in \mathcal{D}_{te}} (v_{i} - \hat{v}_{i})^{2}}{\sum_{i \in \mathcal{D}_{te}} (v_{i} - \bar{v})^{2}},$$
(13)

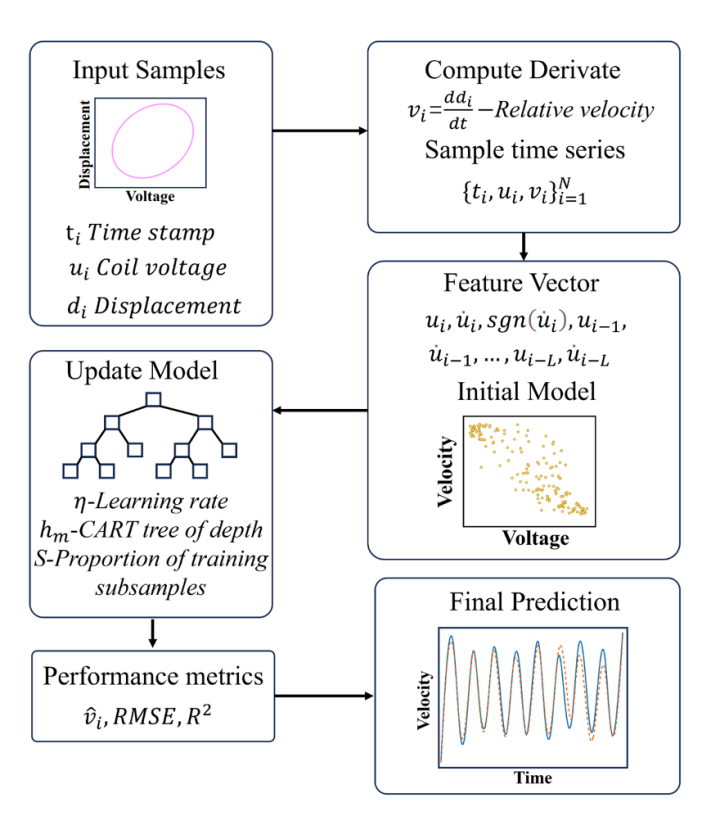


Figure 2. Structure diagram of the self-sensing velocity prediction model of the SS-EMSD based on GBR.

where the closer R^2 is to 1, the better the prediction. And the predicted velocity is:

$$\bar{v} = \frac{1}{|\mathcal{D}_{te}|} \sum_{i \in \mathcal{D}_{t}} v_{i}. \tag{14}$$

The complete mapping is shown in figure 2, which shows the complete data-driven model process from extracting features of the induced voltage (including voltage difference and historical lag terms) to using the GBR algorithm for real-time relative speed prediction.

2.3. Feature selection and parameter optimization of the GBR model

To improve the predictive accuracy of the GBR model under on-board constraints, the voltage-derived features directly from induced EMF in time domain are heeded. Because the coil EMF is proportional to the time rate of change of the flux linkage, the first derivative \dot{u} (implemented as a discrete difference) carries information that is approximately proportional to the relative velocity, while its polarity $\mathrm{sgn}\left(\Delta u_i\right)$ resolves the motion direction. Since the SS-EMSD exhibits hysteresis and circuit/core memory, a short set of lags is included to encode rate- and path-dependent effects.

MI, RFE, and SHAP are commonly used feature selection techniques to quantify the relative contribution of each.

Specifically, the MI was computed between the candidate feature *X* and target velocity *Y* using:

$$I(X;Y) = \sum_{x \in X} \sum_{y \in Y} p(x,y) \log \frac{p(x,y)}{p(x)p(y)},$$
 (15)

where p(x,y) is the joint probability distribution of feature value x and target value y, while p(x) and p(y) are their respective marginal probabilities. This quantity captures the reduction in uncertainty about Y and the given knowledge of X, and thus quantifies the feature information for predicting the target.

In addition to MI, RFE was applied to iteratively prune less relevant features based on feature importance derived from the GBR model. Furthermore, SHAP was utilized to provide a more interpretable and theoretically-grounded quantification of the feature impact. The SHAP value ϕ for a feature i is computed as:

$$\phi_{i} = \sum_{S \subseteq F\{i\}} \frac{|S|! (|F| - |S| - 1)!}{|F|!} \left[f_{S \cup \{i\}} \left(x_{S \cup \{i\}} \right) - f_{S} \left(x_{S} \right) \right].$$
(16)

where F is the full set of input features, S is any subset without containing feature i, and $f_S(x_S)$ is the model's prediction when only features in S are known. The SHAP formulation reflects the average marginal contribution of feature i across all possible feature subsets, weighted by the number of permutations in which the subset appears. This approach ensures a fair and consistent attribution of the prediction to each input feature, grounded in cooperative game theory.

The predictive capability of the GBR model is highly sensitive to its hyperparameters: number of trees (M), learning rate (η) , tree depth (d_{\max}) , subsample ratio (S), and the full set of input features F. To find optimal hyperparameter settings, a grid search combined with 10-fold cross-validation was applied to minimize the empirical loss function:

Best parameters =
$$\arg\min_{\theta \in \odot} \frac{1}{k} \sum_{i=1}^{k} \text{RMSE}_{i}(\theta)$$
. (17)

In parallel, Bayesian optimization was employed as a complementary search strategy to efficiently explore optimal hyperparameter spaces.

2.4. Damping control logic

Figure 3 shows the application principle of SS-EMSD. Following the data-driven identification of the voltage-to-velocity relationship, the prediction model must be embedded in a real-time firmware so that the EMSD can adjust its electrical load online. The microcontroller collects coil voltage samples at a frequency of 50 Hz. Then, the measured voltage

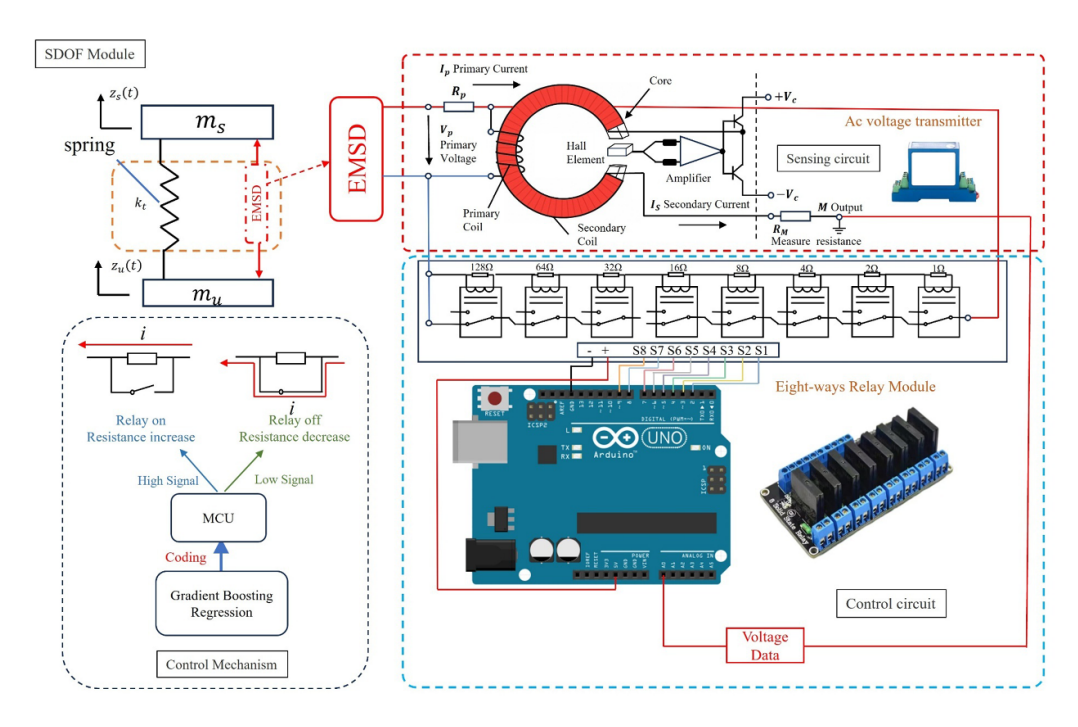


Figure 3. A real-time closed-loop control integrated a single-degree-of-freedom (SDOF) vibration system combined with SS-EMSD, including the control strategy, the electromagnetic damper, and the circuit components.

signals from four rapid analog-to-digital converters are averaged to attenuate quantization noise as

$$u_k = \frac{1}{4} \sum_{i=0}^{3} \frac{ADC_{A0,k,i}}{1023} V_{\text{ref}},$$
 (18)

where V_{ref} is the reference voltage of the firmware.

With a fixed step Δt , the discrete derivative of the averaged voltage can be expressed as

$$\dot{u}_k = \frac{u_k - u_{k-1}}{\Delta t},\tag{19}$$

which provides the directional information for accurate velocity inference (proved in section 3).

To reach the flash constraint of the MCU while preserving the nonlinear accuracy of the GBR model in Section 2.2, the full ensemble is compressed. The real-time calculation of the speed v_k in the MCU is converted to:

$$v_k = \sum_{m=1}^{M'} \gamma_m h_m(\mathbf{X}_k), \qquad (20)$$

where M' is the number of trees after compression, γ_m is scaling weights, and X_k is the voltage feature set except that u_k is collected by the MCU in real time.

In this paper, a balance-logic adaptive damping control is proposed. The essence of balance logic is that the damper is engaged only when the relative displacement x_k and the relative velocity v_k have opposite signs (or $v_k = 0$), i.e. when. Under this condition, the damper functions as the mass moves back toward its equilibrium position. When $x_k v_k > 0$, the damper is

switched off so that it does not inject additional energy into the system.

The inferred status of $\{x_k, v_k\}$ drives the piece-wise damping law to set the control damping force

$$F_{d}(k) = \begin{cases} k_{s} |x_{k}| \operatorname{sgn}(v_{k}), x_{k} v_{k} \leq 0, \\ 0, x_{k} v_{k} > 0 \end{cases}$$
 (21)

where k_s is the balance-logic gain that scales the damping force in proportional to the instantaneous displacement magnitude $|x_k|$; a larger k_s yields a greater real-time damping action.

The balance logic strategy, first introduced by Rakheja and Sankar [39] and later refined by Stammers & Sireteanu [40], is widely adopted for reducing chassis acceleration in semi-active suspensions and adapted to EMSD in this paper.

In the proposed SS-EMSD, the mechanical damping is inversely related to the total circuit resistance; equating with the electrodynamic expression equation (5) yields the target load resistance $R_{\text{calc}}(k)$,

$$R_{\text{calc}}(k) = \begin{cases} 255\Omega & \frac{K_{\text{t}}^{2}}{F_{\text{d}}(k)} v_{k} - R_{\text{in}} > 255\Omega \\ \frac{K_{\text{t}}^{2}}{F_{\text{d}}(k)} v_{k} - R_{\text{in}} & 0\Omega < \frac{K_{\text{t}}^{2}}{F_{\text{d}}(k)} v_{k} - R_{\text{in}} < 255\Omega \\ 0\Omega & 0\Omega < \frac{K_{\text{t}}^{2}}{F_{\text{d}}(k)} v_{k} - R_{\text{in}} \end{cases}$$
(22)

where the adjustable resistance range in this study is 0–255 Ω .

In summary, equations (15)–(19) constitute an integrated firmware workflow that links the statistically inferred voltage-to-velocity mapping to an adaptive damping mechanism. The system measures voltage, predicts velocity in real time, calculates the necessary damping coefficient, converts it to an electrical load, and actuates the corresponding

relay configuration-while broadcasting precise displacement for supervisory monitoring simultaneously. This closed-loop implementation demonstrates that the predictive model can develop earlier transitions into a practical, low-latency control strategy seamlessly for the velocity-adaptive electromagnetic damping adjustment.

3. Experimental setup and parameter identifications

To verify the expected control force tracking and relative velocity prediction performance under excitation, an SS-EMSD prototype was fabricated and installed on the exciter for testing, as shown in figure 4. In this section, the corresponding model parameter identification process is also elaborated in detail.

3.1. Experiment setup

In the experimental platform, an SDOF spring-mass system with SS-EMSD is mounted on a non-contact shaker. The key components comprise an EMSD with the opposed-magnet-column, an eight-channel solid-state relay array, and an adjustable resistor network. All components are rigidly affixed to an optical table to ensure the smooth experimental operation of the system. Excitation signals are produced by a signal generator and amplified by a power amplifier. Then the non-contact exciter is driven to shake under specific waves, thereby inducing relative motion in the upper mass-spring-EMSD assembly. A variable resistor connected with the EMSD coil in series is governed by Arduino UNO R3 (an MCU switches the relays in real time), discretely adjusting the external load resistance to generate the required damping force specified by the control algorithm.

To realize the real-time damping-force control with the self-sensing capability, the acquisition of the EMSD state has been shifted from an external laser displacement sensor to an AC voltage transducer. The coil voltage is first rectified and filtered to obtain an equivalent DC RMS value. This signal is then galvanically isolated by the voltage transducer and converted into the coil's relative velocity by the MCU, which serves as the sole state variable of the closed loop. Consequently, the control loop is completely freed from external displacement or acceleration sensors, reducing energy consumption and eliminating additional assembly errors. Two HG-C1100 laser displacement sensors are retained exclusively for off-line validation: after each experiment, the displacement-velocity sequences measured by these sensors are compared with the self-sensed velocity by SS-EMSD to assess damping force tracking errors.

The adopted balance logic strategy is a real-time damping-force control scheme. During every sampling period, the MCU reads the coil relative velocity provided by the AC voltage transducer and immediately calculates the desired damping force. Relay switching follows a forward look-up table: within a 0.1 s update interval, the MCU selects the next resistance level that minimizes the squared error between the previous desired force and the attainable discrete force. Therefore,

a real-time approximation of the target damping curve is achieved without altering the underlying damping-force computation. The remaining equipment for the experimental test is listed in table 1.

3.2. Model parameters identification

When the platform is excited by a swept-sinusoidal wave from 0.1 Hz to 10 Hz, the measured response curve of the SDOF system is plotted in figure 5 to obtain the characteristics of the system. As the excitation frequency increases, the vibration amplitude of the system gradually increases and reaches a peak at the natural frequency of the SDOF system (about 5 Hz), then decreases after crossing the resonant peak. Figure 5 illustrates the frequency response of the SDOF system in the open-circuit condition, which exhibits the classical bell-shaped amplitude profile typical of a lightly damped system, where the peak appears at the natural frequency due to resonance. In order to verify the resonance suppression and energy harvesting performance, this experiment is conducted with the excitation frequency band around 5 Hz.

4. Training on self-sensing data

This section describes the formulation, training, and validation of the voltage-to-velocity model; reports cross-validated performance metrics; and specifies the compression strategy that enables embedded deployment with a 32-KB memory constraint.

4.1. Model training

In this section, the training procedure and performance evaluation of the voltage-velocity mapping model based on GBR are presented. Firstly, the measured signal samples are used to extract the time series t, the coil induced voltage u, and the true velocity v calculated by the laser displacement sensor and smoothed by the first derivative as shown in figure 6. Unlike conventional force-displacement hysteresis, the voltage-velocity loop captures the nonlinear conversion effects in the electromagnetic domain, as the coil EMF is induced by the relative motion within a spatially varying magnetic field. To express the hysteresis and memory effects explicitly in the model, all the sample points should contain the current voltage u_k , its time derivative \dot{u}_k , direction symbol $\mathrm{sgn}(\dot{u}_i)$, and the fourth-order lag $\{u_{k-l}, \dot{u}_{k-l}\}_{l=1}^4$ dimensions of characteristic vector X_k .

To estimate the relative velocity of the EMSD accurately from the measured voltage, a GBR model is developed and optimized. The raw dataset includes voltage signals u(t), time sequences t, and the corresponding ground-truth velocity v(t). To weigh the model accuracy, a set of 14 derived features was constructed, incorporating the first and second-order voltage derivatives $(du/dt, d^2u/dt^2)$, moving statistics, polarity sign, and up to four lagged terms. The contribution of each feature was first assessed using two ranking strategies: MI and RFE. As shown in figure 7(a), the MI analysis indicates that the derivative-related features contribute most significantly to

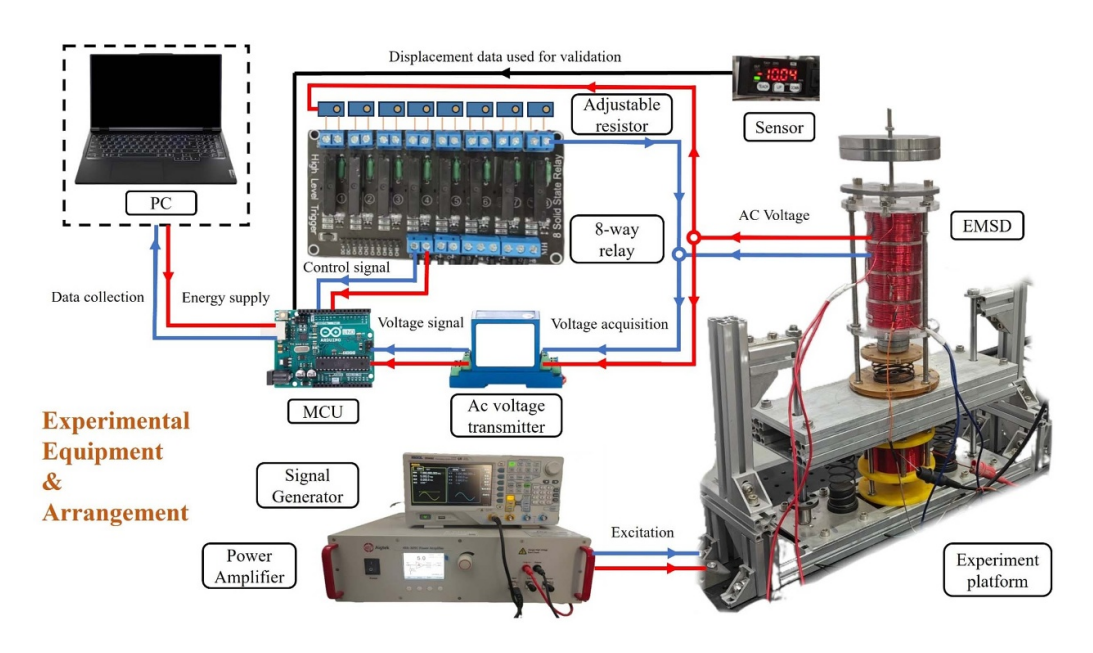


Figure 4. Experimental setup of the SDOF vibration system with the proposed SS-EMSD.

Table 1. Component parameters.

No.	Equipment name	Model and specifications
1	Microcontroller	Arduino UNO R3
2	Sensors	Panasonic HG-C1100
3	Digital oscilloscope	PIGOL DS4082
4	Power amplifier	Aigtek ATA-309 C
5	24 V sensor battery	Taiwan Mean Well DC Switching
		Power Supply LRS-50-2
6	Adjustable resistor	3296 W potentiometer, adjustable
		range 0–200 Ω
7	AC voltage transmitter	Anhui Qidian AC voltage transmitter
		customized version
8	Solid-state relay module	Shenzhen Risym, 8-channel 5 V
	·	high/low level solid-state relay

velocity prediction. Furthermore, RFE results in figure 7(b) confirm that the selected 8 optimal features include all high-value derivative and lag terms, which supports their importance in mapping the measured voltage to the velocity.

Subsequently, the dataset was divided into training and test sets (\mathcal{D}_{tr} : $\mathcal{D}_{te} = 80\%$: 20%), and a 10-fold cross-validated grid search was conducted to tune the GBR model. The optimal hyperparameters were: the learning rate, the maximum tree depth $d_{max} = 4$, the number of estimators M = 400, and the subsampling ratio 0.8. The model converges quickly with squared loss training, which is also evaluated on the test set.

As shown in figure 8, the averaged cross-validation RMSE across folds is 0.02313 m s⁻¹, and the standard deviation is 0.00758 m s⁻¹. The averaged cross-validation RMSE results are consistently low, which validates the model's generalization capacity and confirms the absence of overfitting.

Further testing for the velocity reconstruction task is illustrated in figure 9, which compares the true velocity against the predicted results. In figure 9(a), the standard GBR model shows good agreement in both amplitude and phase, although minor underestimation is visible between 3.10–3.20 s. To

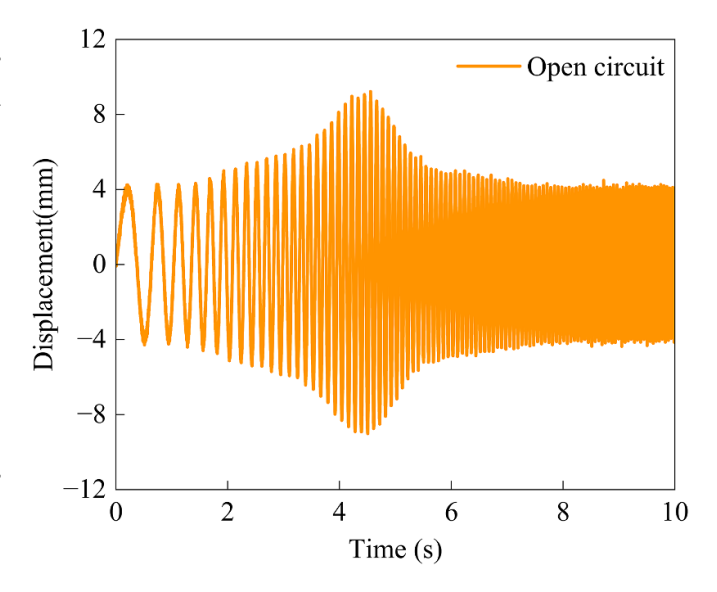


Figure 5. Displacement response of the SDOF system with swept sinusoidal excitation.

enhance alignment, the GBR model is optimized in figure 9(b). Compared with the traditional $R^2 = 0.921$ and RMSE of $0.04035 \,\mathrm{m \, s^{-1}}$, the final model achieves a determination coefficient $R^2 = 0.942$ and a test-set RMSE of $0.03461 \,\mathrm{m \, s^{-1}}$. The prediction error is reduced by 14% versus the traditional GBR model, which is well within the accuracy bounds for real-time damping control.

4.2. Application of self-sensing model in MCU

The selected MCU for this experiment is Arduino UNO R3, whose internal Flash memory size is only 32KB. To meet the 32 KB flash constraint of the Arduino UNO R3 while preserving the nonlinear accuracy of the GBR model in Section 2.2, the full ensemble is compressed rather than

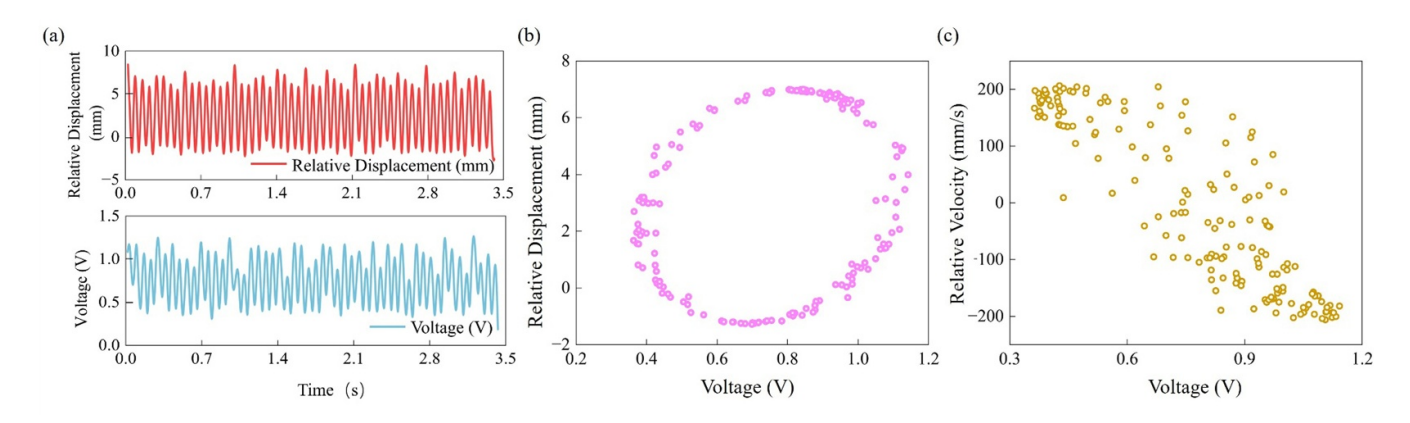


Figure 6. Comparison of the hysteresis characteristics and the prediction accuracy verified by the velocity prediction model of the proposed SS-EMSD: (a) time-domain origin data of voltage and relative displacement; (b) hysteresis loop diagram between the induced voltage measured in the experiment and the real speed of the electromagnetic damper; (c) raw relationship data of relative speed and voltage.

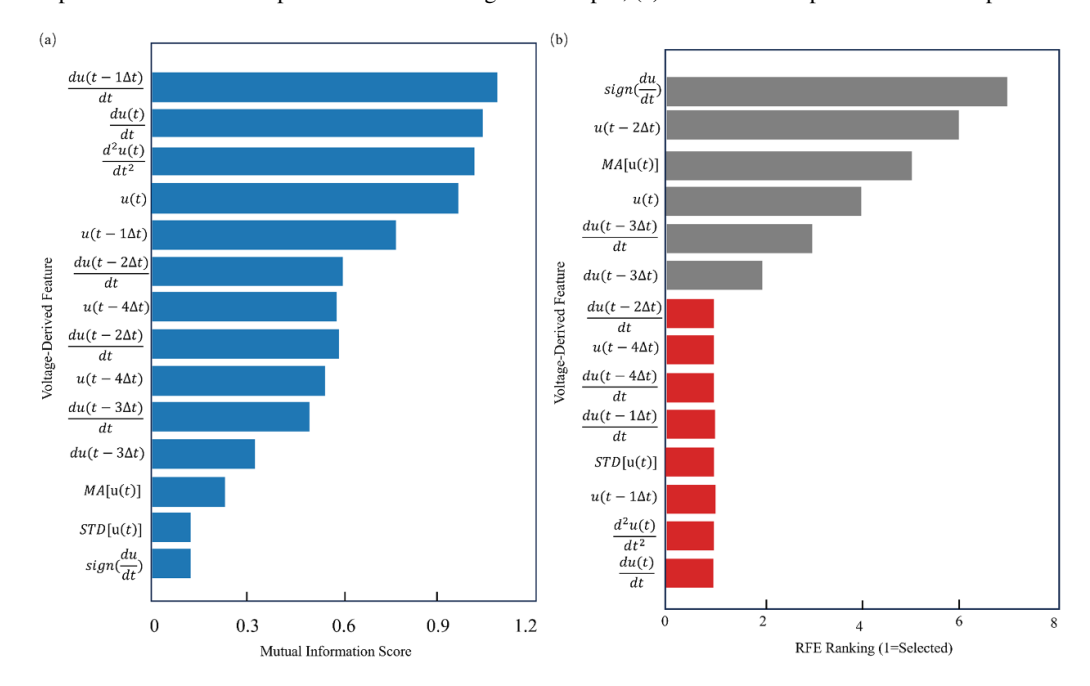


Figure 7. Feature selection results: (a) feature importance based on MI; (b) ranking results from RFE, where red bars indicate selected features. (MA [u(t)] is moving average of voltage u(t), STD [u(t)] is standard deviation in sliding window and Δt is time step between samples).

retrained. Each tree depth is pruned to less than 3, corresponding thresholds and leaf values are quantized to 16-bit signed integers, which reduces the MCU memory by 84%. The remaining M' trees are exported as a sequence of 'if-else' statements through a code-generation script, so the MCU only executes integer comparisons and additions. The runtime complexity for evaluating the ensemble is O(M'd), where M' is the number of compressed trees and d is the maximum tree depth. The complexity corresponds to approximately 45 comparisonand-addition operations per sample, which remains well below the 20 ms sampling interval of the MCU. In this way, the original GBR mapping is evaluated on board with almost no loss of the test-set obtained offline. The code generation was performed with micro-GBDT (gradient boosting decision tree in Python script, open source); the resulting C header occupies 8.2 KB in flash and 520 bytes in SRAM (static random-access memory), which is well within UNO R3 limits. Compared with the linear surrogate (), the compressed-GBR keeps the full nonlinear mapping ($R^2 = 0.942$) as shown in figure 6(b). And the increased instruction cycle (less than 5 μ s) has a considerable performance improvement on the closed-loop vibration control. Finally, the red feature item in figure 7(b) is selected as the reference feature for prediction. In addition, considering the hardware limit of the electromagnetic damper, the initial balance logic parameter k_s is set to 8 N m⁻¹. The remaining parameters are listed in table 2.

5. Experimental results and discussion

In order to validate the theoretical model and verify the feasibility of the system, experiments are required. With the

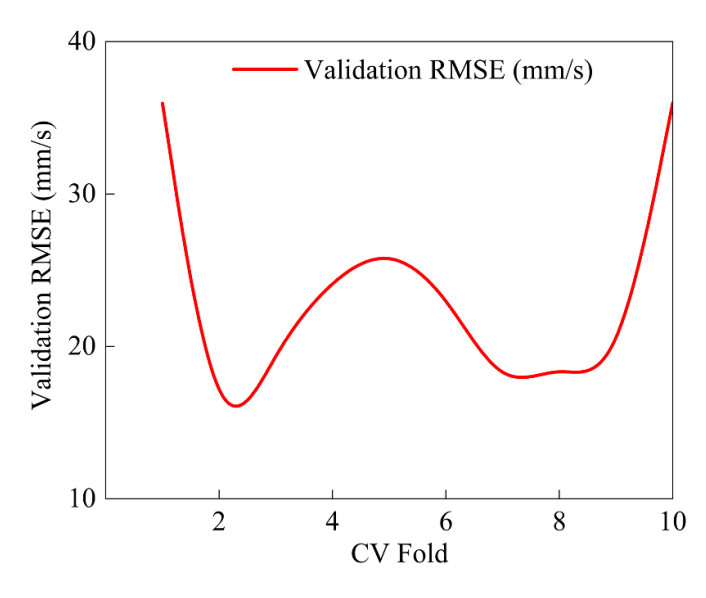


Figure 8. Validation RMSE across 10 folds using the optimal GBR configuration.

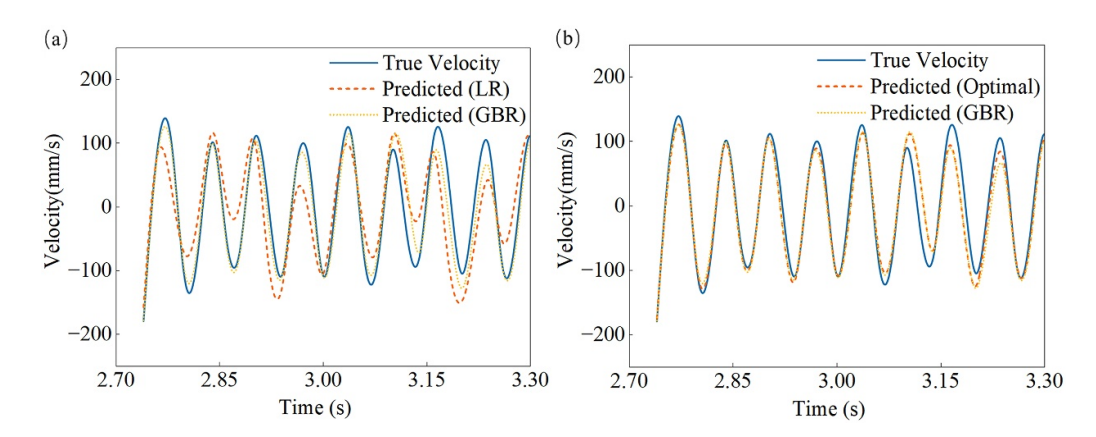


Figure 9. Comparison of predicted velocity and ground truth in the test interval [2.70, 3.30] s: (a) baseline GBR model; (b) optimized GBR model showing improved fit in both amplitude and phase.

Table 2. Identified parameters.

System	Notation	Value
	$m_{ m s}$	3.2787 kg
	m_u	0.0423 kg
EMSD	k	640 N m^{-1}
	K_{t}	34
	$R_{\rm in}$	$0.8~\Omega$
	$V_{ m ref}$	5 V
	M	400
	η	0.03
Self-sensing	R^2	0.942
	RMSE	0.03461 m s^{-1}
	M'	15
	$k_{\rm s}$	8 N m^{-1}

experimental setup in section 3 and the identified system parameters in section 4, the measured experimental results are analyzed in this section.

5.1. Vibration suppression performance using the balance logic

The experimental validation for the SS-EMSD was comprehensively conducted with the 1–10 Hz excitation. The displacement responses under both controlled conditions (balance logic and open circuit) are shown in figures 10–12. Since the mass effect is dominant rather than the damping effect in the low-frequency range (1–2 Hz in figure 10), there is no effective vibration reduction in this frequency range.

The vibration attenuation is particularly evident when the excitation is near the system's natural frequency. The vibrational amplitude is approximately decreased from 3 mm to 2 mm after the damping is tuned with the balance logic control strategy. In the intermediate frequency spectrum (3–6 Hz, figure 11), the system shows robust suppression performance continuously and consistently.

After crossing the resonant peaks, the tunable damping is still effective, but not as good as the resonant frequency range. Particularly, the balance logic control strategy shows adaptive capability for the higher frequencies (7–10 Hz) as shown in

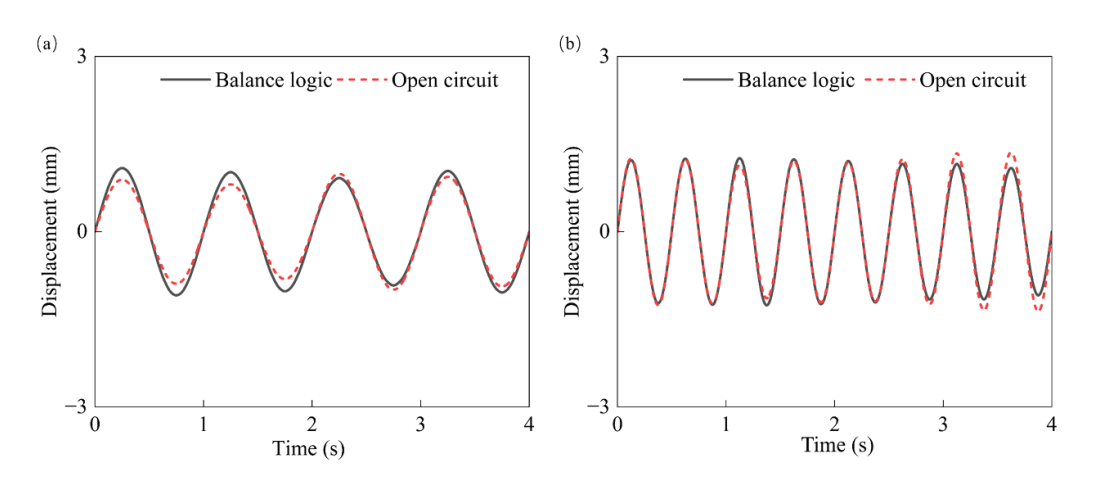


Figure 10. The displacement response curves with the 1–2 Hz sinusoidal excitation.

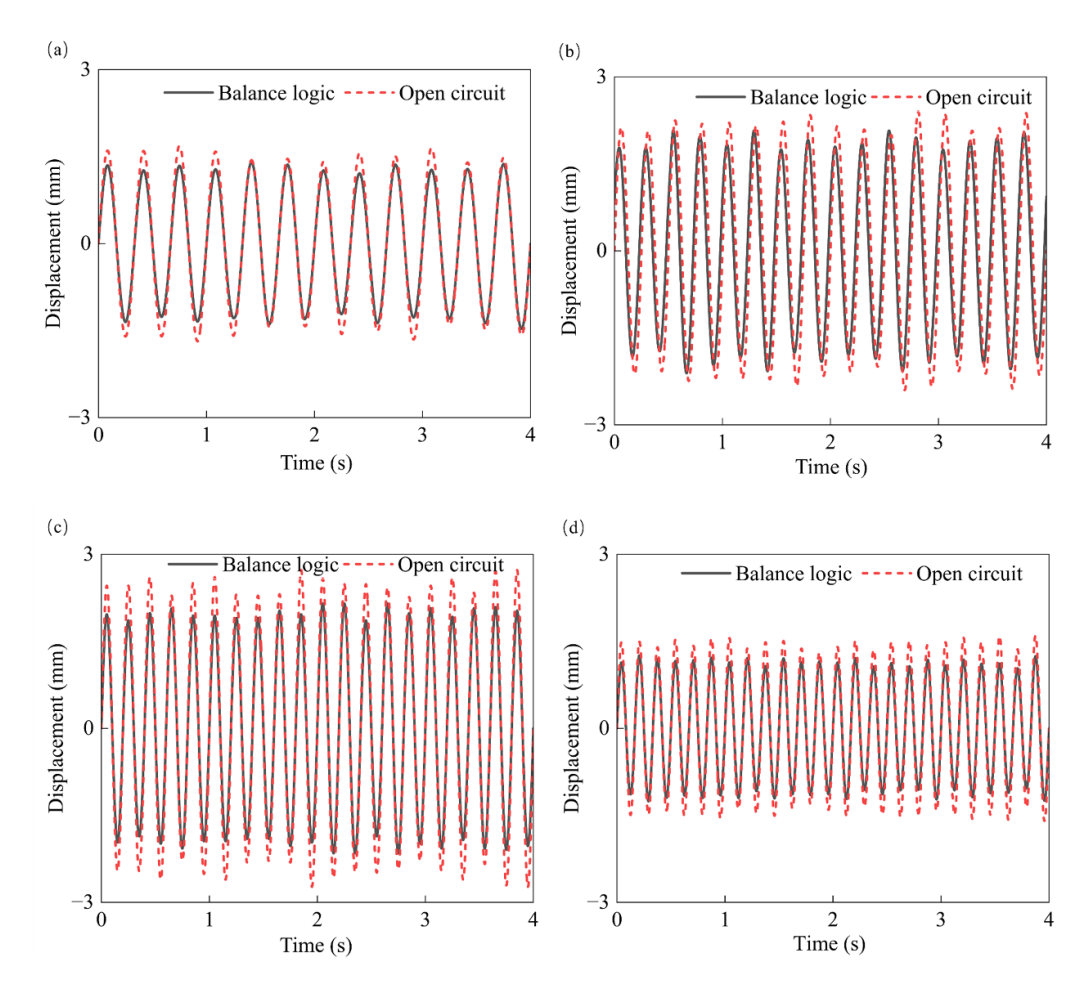


Figure 11. The displacement response curves with the 4–6 Hz sinusoidal excitation.

figure 12. The vibration response amplitude is cut by almost half with 10 Hz sinusoidal excitation.

The vibration control sustains its damping efficiency, albeit with slightly diminished magnitude, further highlighting the robustness and broad-spectrum adaptability of the balance logic mechanism. Overall, a peak vibration attenuation of approximately 15% at resonance and an average suppression consistently exceeding 10% across the tested frequency range,

which confirms the significant practical implications of the proposed SS-EMSD system.

5.2. Velocity prediction performance

The velocity predicted by the GBR model and the actual measured velocity obtained from high-precision laser displacement sensors are compared in figure 13. These results clearly

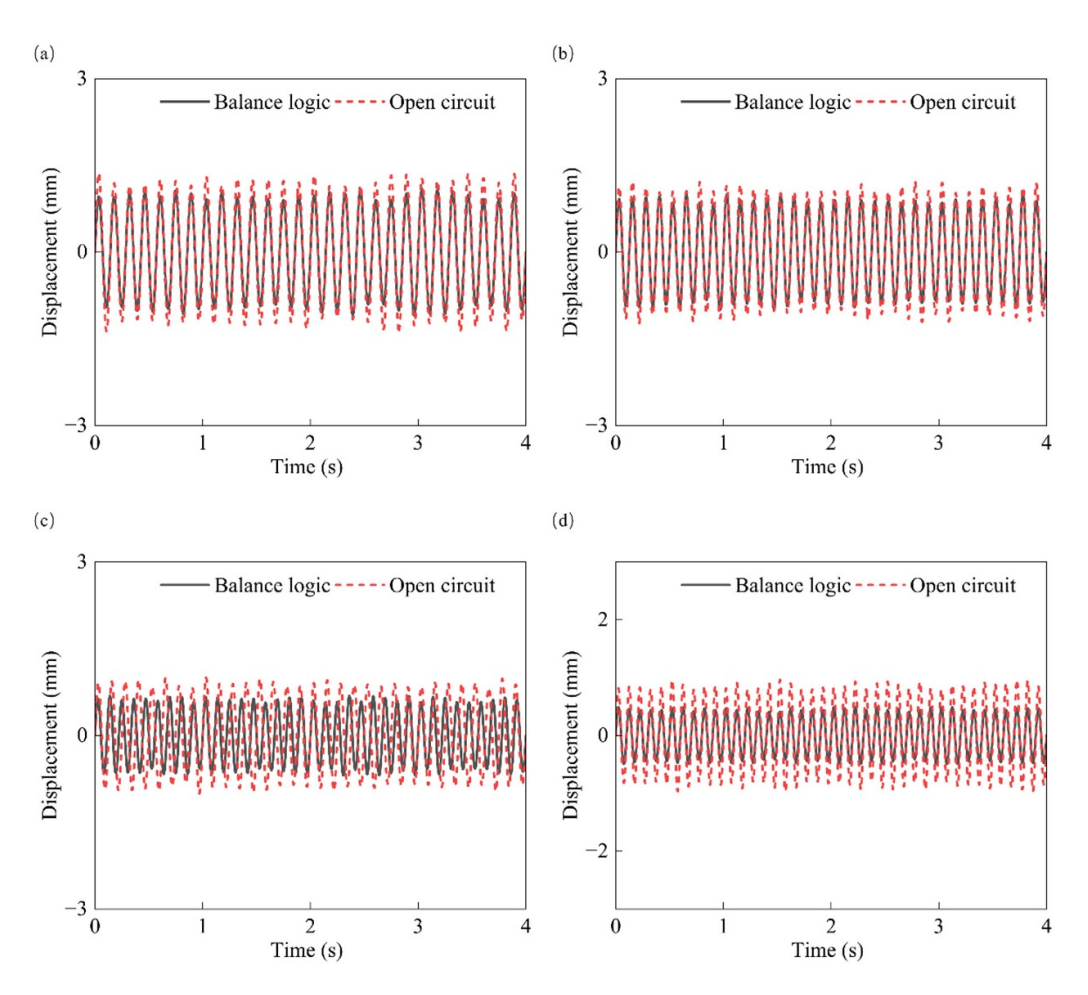


Figure 12. The displacement response curves with the 7–10 Hz sinusoidal excitation.

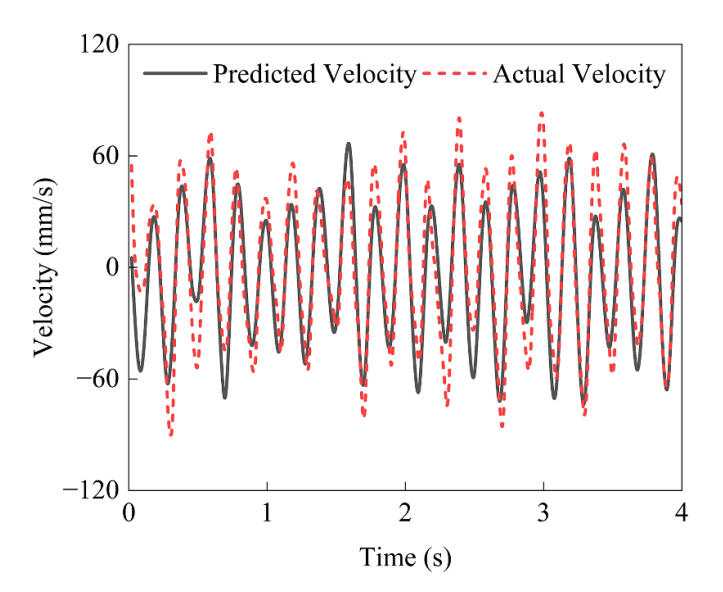


Figure 13. Velocity prediction accuracy performance evaluation of damping force under 5 Hz excitation condition: detailed comparison between the real-time predicted speed of the model and the real speed waveform measured in the experiment.

underscore the model's advanced capability of reconstructing the SS-EMSD relative velocity with remarkable precision in terms of both amplitude and phase alignment. Even with minor deviations during transient dynamics, the phase consistency is preserved at over 85% accuracy, demonstrating reliable alignment between predicted and measured waveforms. The

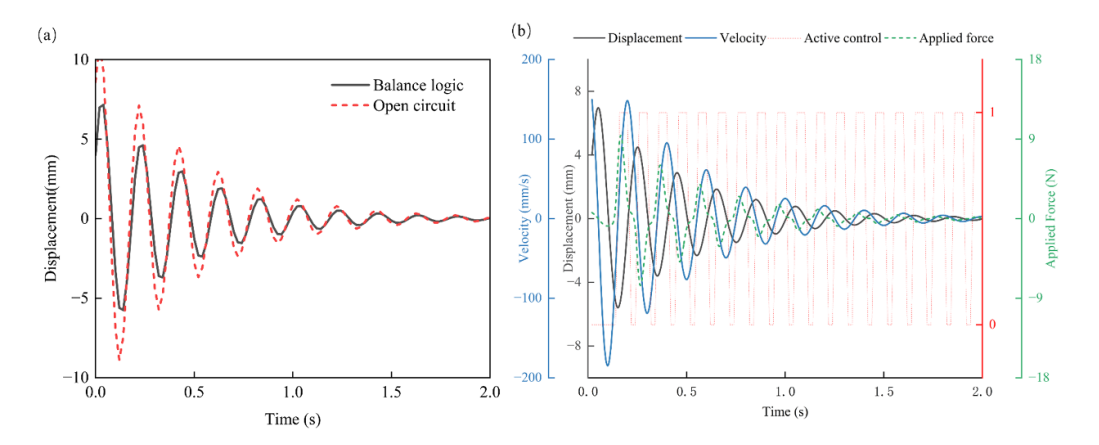


Figure 14. The system response with step excitation, (a) displacement response under step excitation with and without balance logic control, (b) detailed comparison of displacement, velocity, and damping force in active control state.

high phase fidelity strengthens confidence in the model's suitability for real-time control and validates the efficacy of the data-driven approach for accurate, dependable embedded velocity inference.

5.3. Step excitation response

This section illustrates the SS-EMSD system's dynamic response with the step excitation, assessing its robustness and adaptability under unpredictable and variable vibrational scenarios. When the system is under step excitations, the response curves in figure 14(a) reveal that the SS-EMSD system can reduce the vibration amplitudes significantly compared to the uncontrolled open-circuit case.

The balance logic algorithm, which tunes the damping force application based on the signs of relative displacement and relative velocity, plays a crucial role in this performance. As shown in figure 14(b), the damper is activated and exerts a damping force when the relative displacement and relative velocity have opposite signs. During this system's energy absorption phase, the damper reduces the vibrational amplitude and dissipates the dynamic energy effectively. Conversely, when displacement and velocity share the same sign, indicating that the damper would not function, the balance logic deactivates the damping force to prevent unintended energy addition. This selective engagement of the damper effectively maximizes energy dissipation during energy absorption phases and minimizes detrimental energy input during release phases, enhancing the overall efficiency and stability of the vibration control.

The response amplitude is considerably minimized in figure 14, demonstrating the system's capability of adapting to the rapidly varying conditions with the strategic control logic strategy. The inherent robustness and the rapid adaptive control capability highlight the practical applicability and reliability of the proposed self-sensing damping control strategy. Such consistent performance under step excitation validates the potential deployment of the SS-EMSD system in real-world scenarios characterized by stochastic and non-deterministic vibrational disturbances.

To summarize, the comprehensive experimental results in figures 10–14 thoroughly validate both the theoretical model and the practical efficacy of the proposed SS-EMSD system. These results underscore the damper's exceptional adaptability, superior vibration attenuation capabilities, and reliable real-time control performance across an extensive frequency range.

The experiments discussed in this study are conducted within 1–10 Hz, which covers the dominant resonance of the SDOF test rig used in this paper. All sensing and control results should therefore be interpreted within this frequency band. The proposed self-sensing and damping mechanism is not intrinsically limited to a particular frequency range. The data-driven mapping and control parameters, however, need to be identified for the target frequency bands. When moving to frequencies far from the trained band or multi-mode structures, re-identification and re-training would be required, leading to different performance. A rigorous evaluation outside 1–10 Hz is beyond the scope of this work and will be addressed in future studies on broader frequency bands using multi-mode test rigs.

6. Conclusions

This paper proposes a SS-EMSD combined with a physically informed GBR model to achieve adaptive vibration control with the balance logic. The GBR model predicts relative velocity directly from the SS-EMSD voltage and drives online damping adjustment without external displacement or acceleration sensors. This predicting process simplifies the control architecture while preserving adaptability. Experiments on the test rig show that the proposed system entails over 10% average vibration-amplitude attenuation across non-resonant frequencies and up to 15% at resonance, while capping the prediction accuracy over 85%. Results also indicate that the sensing accuracy is adequate for closed-loop semi-active control and the proposed integrated SS-EMSD offers an efficient and practical solution for precision vibration mitigation. Future work will extend the evaluation to broader working frequency

bands, multi-mode configurations. The proposed methodology can also be further refined for embedded implementation toward robust, long-term field deployment.

Data availability statement

The data cannot be made publicly available upon publication because no suitable repository exists for hosting data in this field of study. The data that support the findings of this study are available upon reasonable request from the authors.

Acknowledgments

This work was supported by the National Natural Science Foundation of China (Grant No. 52505087), the Natural Science Basic Research Program of Shaanxi Province (Grant No. 2024JC-YBQN-0523), and the Shaanxi Province Postdoctoral Science Foundation (Grant No. 2023BSHEDZZ214). This work was also partially supported by grants from the RIAIoT (Research Institute for Artificial Intelligence of Things) through project P0049625.

Author contributions

Qiheng Xu 0 0009-0008-9133-3260

Data curation (lead), Formal analysis (lead), Investigation (lead), Methodology (lead), Writing – original draft (lead)

Ruqi Sun D 0000-0002-5926-8971

Conceptualization (lead), Funding acquisition (lead), Methodology (equal), Resources (lead), Supervision (lead), Writing – review & editing (equal)

Yongjia Liu

Data curation (equal), Investigation (supporting)

Oian Li

Investigation (supporting), Writing – review & editing (supporting)

Li Cheng 0 0000-0001-6110-8099

Funding acquisition (equal), Supervision (equal), Writing – review & editing (equal)

References

- [1] Li J Y and Zhu S 2021 Tunable electromagnetic damper with synthetic impedance and self-powered functions *Mech. Syst. Signal Process.* 159 107822
- [2] Shen W et al 2022 Energy harvesting performance of an inerter-based electromagnetic damper with application to stay cables Mech. Syst. Signal Process. 170 108790
- [3] Li D et al 2025 Feasibility of eddy current damping-based tuned mass damper inerter for a nonlinear hybrid base-isolated building J. Build. Eng. 104 112231
- [4] Sun K, Tang J, Wu Z, Li Y and Cao D 2024 Coupled nonlinear vibration characteristics of quasi-zero-stiffness Gough-Stewart isolation platform *Aerosp. Sci. Technol.* 152 109352

- [5] Sun K et al 2024 Active control of quasi-zero-stiffness vibration isolator with variable load Int. J. Struct. Stab. Dyn. 24 2450243
- [6] Tan B et al 2025 Cooperative compensation control for a novel semi-active electromagnetic suspension integrating with variable damper and variable inertance Mech. Syst. Signal Process. 226 112344
- [7] Sun R and Wong W 2019 Vibration control with a tunable self-sensing electromagnetic shunt damper 23rd Int. Conf. on Mechatronics Technology (ICMT) pp 1–6
- [8] Zaccardo V M and Buckner G D 2023 Saturation and duty cycle tolerant self-sensing for active magnetic dampers Mech. Syst. Signal Process. 200 110567
- [9] Cui J, Bai S, Li X, Jia L, Li G, Zheng Y and Xue C 2023 Integration of triboelectric sensing and electromagnetic energy harvesting for self-adaptive vibration suppression *Nano Energy* 113 108525
- [10] Tang M, Fang Z, Fan C, Zhang Z, Kong L, Chen H, Zeng Z, Yang Y and Qi L 2025 An AI-driven electromagnetic-triboelectric self-powered and vibration-sensing system for smart transportation *Eng.* Struct. 323 119275
- [11] Shen H, Ji H, Qiu J, Yang Q, Yu M, Bian Y and Ding X 2021 Self-powered semi-passive vibration damping system based on the self-sensing approach *J. Sound Vib.* **512** 116371
- [12] Qin A, Zhang B, Ning D, Tan B and Du H 2024 A self-sensing approach for estimating suspension displacement and velocity in semi-active electromagnetic dampers *Mech. Syst. Signal Process.* 208 111049
- [13] Hong F and Pang C K 2012 Robust vibration control at critical resonant modes using indirect-driven self-sensing actuation in mechatronic systems ISA Trans. 51 834–40
- [14] Freyer B H, Theron N J, Heyns P S and Pickelmann L A 2021 Self-sensing active control of emulated tangential tool vibration *Control. Eng. Pract.* 109 104729
- [15] Li Z, Zhang J, Feng P, Yu D, Lan T and Wang J 2025 Development of an ultrasonic elliptical vibration chiseling device with trajectory self-sensing capability *Measurement* 245 116628
- [16] Mao Y and Dankowicz H 2024 On a principle for mass sensing using self-excited template dynamics of coupled oscillators and root-finding algorithms J. Sound Vib. 571 118027
- [17] Li Z et al 2025 Self-sensing sliding mode control of workpiece chatter based on accurate prediction of machining vibration J. Sound Vib. 600 118887
- [18] Chang L-K et al 2018 Impedance control of self-sensing piezoelectric actuator for vibration suppression Proc. ICEMS p 2533
- [19] Hu H *et al* 2007 Active vibration control by piezoelectric self-sensing actuator for beam under a moving mass *Proc. ICEMI* vol 3 pp 600–1
- [20] Bao B and Tang W 2017 Semi-active vibration control featuring a self-sensing SSDV approach *Measurement* 104 192–203
- [21] Cao J et al 2015 Semi-active vibration control using self-sensing synchronized switch damping on negative capacitance Proc. CCC p 5753
- [22] Jiang J, Tang J, Sun K, Chen H, Li Y and Cao D 2025 Data-driven model identification and control of the quasi-zero-stiffness system *Nonlinear Dyn.* 113 3999–4013
- [23] Neubauer M, Hinze C and Verl A 2025 Semi-active damping for industrial robots *Robot. Comput. Integr Manuf.* 95 103008
- [24] Zhang H, Wang L and Shi W 2025 Semi-active variable stiffness and damping control for adjacent structures using LSTM-based prediction algorithm *J. Build. Eng.* 103 112127
- [25] He W, Zhou Y, Xu H, Shang F and Liu W 2025 Shaking table test and seismic evaluation of cross-layer installed

- cable-bracing displacement amplification damped system *J. Build. Eng.* **103** 112040
- [26] Lai Z, Liu Y, Tan P, Peng J and Zhou F 2025 A semi-explicit integration algorithm with controllable numerical damping for real-time hybrid simulation *Structures* 74 108606
- [27] Yan B, Wang S, Ling P, Yang Z, Ma H and Li Q 2025 Seahorse-exoskeleton-inspired structure with linear-to-torsion transition property for low-frequency vibration isolation *Fund. Res.* 5 1505–23
- [28] Bao C et al 2025 A novel horizontal universal viscous damping amplification device and seismic response analysis Soil Dyn. Earthq. Eng. 188 109062
- [29] Yang D *et al* 2025 Dynamic response reduction of floating offshore renewable energy applications with a high-damping mooring system *Ocean Eng.* 324 120609
- [30] Nasiri K and Moradi H 2025 Nonlinear milling of a flexible plate-workpiece with tool wear & process damping: bifurcation, stability analysis, and chatter suppression via tunable vibration absorbers *Thin-Walled. Struct.* 210 113017
- [31] Zhang Y *et al* 2025 Stability and dynamic response of centrifugal pendulum vibration absorber based on nonlinear hybrid damping *J. Sound Vib.* **600** 118869
- [32] Cui Y et al 2025 Bio-inspired structures for energy harvesting self-powered sensing and smart monitoring Mech. Syst. Signal Process. 228 112459

- [33] Xu H and Zhou S 2025 Theoretical and numerical investigation of the nonlinear "V" to "U" typed monostable energy harvester under random excitation *J. Comput. Nonlinear Dyn.* 20 091008
- [34] Tan D et al 2025 A cylindrical bistable hybrid triboelectric-electromagnetic energy harvester for harvesting low-frequency vibration energy Energy 334 137597
- [35] Ma X et al 2022 Characterizing nonlinear characteristics of asymmetric tristable energy harvesters Mech. Syst. Signal Process. 168 108612
- [36] Zeng L et al 2024 A self-powered and self-sensing hybrid energy harvester for freight trains Sustain. Energy Technol. Assess. 71 104004
- [37] Zhu Z, Wang Z, Dai K, Wang X, Zhang H and Zhang W 2023 An adaptive and space-energy efficiency vibration absorber system using a self-sensing and tunable magnetorheological elastomer *Nano Energy* 117 108927
- [38] Tian G, Gong X, Xia M, Gong D, Qi K, Liu C, Wang R and Wei K 2025 Active control of low-frequency vibrations with parameter self-optimization for quantum sensing *Measurement* 251 117195
- [39] Rakheja S and Sankar S 1985 Vibration and shock isolation performance of a semi-active "on-off" damper *J. Vib.* Acoust. 107 398–403
- [40] Stammers C W and Sireteanu T 1998 Vibration control of machines by use of semi-active dry friction damping J. Sound Vib. 209 671–84